Design and Optimization of Wide-Coupling Nested Magnetic Coupling Mechanism for UAV Wireless Power Transfer

Ming Xue, Yanjie Guo, *Member, IEEE*, Weida Xu, Yibo Gao, and Shengyan Qiu

***Abstract*—Within the UAV sector, wireless power transfer applications face challenges due to inaccuracies in landing positioning and docking control, leading to misaligned docking and variable offset ranges. The existing magnetic coupling mechanisms offer limited power supply areas, insufficient to meet the demands of random loads across a wide range of positions. This article focuses on the magnetic coupling mechanism of UAV wireless power transfer systems and proposes a nested UAV wireless power transfer system for a broad coupling region to expand the power supply area and ensure stable power distribution. Employing finite element numerical analysis, the spatial magnetic field generated by the nested emission module is examined, revealing the distribution characteristics of magnetic induction intensity above the module. A "cross-shaped" compensation coil is designed to address coupling blind spots within the power supply area. A coupling performance evaluation method based on optimal magnetic coupling regions is introduced to determine the optimal parameters for the nested magnetic coupling mechanism, along with a general expansion process for multistage embedded coils. Furthermore, by analyzing the cross-coupling state between receiving coils, the spatial arrangement of the receiving end coils is delineated, and their structural parameters are established. An experimental platform for the nested UAV wireless power transfer system is constructed, demonstrating that within the proposed optimal coupling region, power fluctuations are less than 25%, and the magnetic coupling mechanism provides a wide, stable, and reliable power reception area for random loads.**

***Index Terms*—Broad coupling region, nested magnetic coupling mechanism, optimal coupling region, UAV wireless power transfer system.**

I. INTRODUCTION

THE UAV wireless power transfer technology is usually based on research related to static wireless charging, and realizes real-time power supply to random loads by improving magnetic coupling mechanisms [1], [2], [3], compensation topology networks [4], [5], [6], [7], and system control strategies [8], [9], [10], [11]. Due to the real-time positional changes of the random load with respect to the energy transmitting end, the even distribution of magnetic fields at the transmitting end is a prerequisite for stable operation of the receiving end. The distribution of magnetic fields is mainly directly related to the physical parameters and external characteristics of the magnetic coupling mechanism. Therefore, research on magnetic coupling structures is of great significance for the stability of the UAV wireless charging systems [12], [13], [14], [15].

Current scholarly discourse, both domestically and internationally, is primarily concentrated on the magnetic coupling mechanisms of dynamic wireless power supply systems, which are categorized into long-guide rail [16], [17], one-dimensional (1-D) array [18], [19], and 2-D array configurations [20], [21], [22], [23]. In the long-guide rail type, the transmitter coil typically exceeds the receiver coil in length. This design offers the advantage of simplified control requirements, reduced complexity, and lower costs. However, it is not without its drawbacks, such as increased electromagnetic radiation and a limited transmission range [16], [17]. To mitigate system leakage and augment transmission efficiency, the transmitter in a wireless power transfer system can be composed of multiple coils arranged in a 1-D array along the direction of load movement, controlled according to the load's position. Nonetheless, this necessitates in-depth research into derived receiving end parameter fluctuations [18], [19], switching control mechanisms [24], [25], and load position detection techniques [26], [27].

While 1-D array technology significantly improves system transmission efficiency, it restricts the trajectory of load movement and is ill-suited for scenarios requiring wireless power reception at arbitrary load locations. Zhang et al. [20] introduced a circular coil as the fundamental transmitting unit, constructing an arrayed power transmission mechanism that, through the superposition of physical positions of the minimum transmitting unit, generates a stable spatial magnetic field, thereby facilitating stable power reception over a broad range of load movement. Xue et al. [21] addressed the power supply needs of robots by defining partition methods for the effective coupling area, establishing a spatial distribution pattern for a 2-D arrayed transmitting module and its corresponding coil excitation conduction mode, thus meeting the real-time power supply requirements

Received 11 July 2024; accepted 31 August 2024. Date of publication 25 September 2024; date of current version 26 May 2025. This work was supported by the National Natural Science Foundation of China (General Program) under Grant 52077153. Recommended for publication by Associate Editor F. Costa. *(Corresponding author: Weida Xu.)*

Ming Xue, Yanjie Guo, Weida Xu, and Shengyan Qiu are with the State Key Laboratory of Reliability and Intelligence of Electrical Equipment, Hebei University of Technology, Tianjin 300401, China, and also with the Hebei Key Laboratory of Equipment and Technology Demonstration of Flexible DC Transmission, Hebei University of Technology, Tianjin 300401, China (e-mail: xueming@hebut.edu.cn; yjguo@hebut.edu.cn; 202411401013@stu.hebut.edu.cn; 202331402061@stu.hebut.edu.cn).

Yibo Gao is with the Tianjin University of Technology, Tianjin 300384, China (e-mail: 2131070878@tiangong.edu.cn).

Color versions of one or more figures in this article are available at https://doi.org/10.1109/TPEL.2024.3455354.

Digital Object Identifier 10.1109/TPEL.2024.3455354

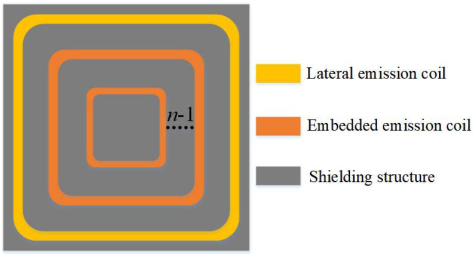

Fig. 1. Schematic diagram of nested transmitting module.

across the entirety of the robot's operational space. Tan et al. [22] proposed a multitransmitter coupling structure based on a hexagonal array coil, creating a uniformly distributed magnetic flux at the transmitter through seamless stitching. Utilizing the coupling characteristics between coils, a flexible switching control strategy for the minimum transmitting unit is introduced, enhancing transmission efficiency at coil boundaries compared to circular and square array coils. Li et al. [23] presented an array structure with a regular arrangement of bipolar and unipolar coils, achieving natural decoupling of the two coils and maintaining stable coupling between the transmitting array and receiving coils during movement, ensuring a stable output power. Despite the 2-D array wireless power transfer system offering a substantial power supply area, challenges persist at the transmitter, including a complex system structure, stringent control accuracy requirements, and elevated application costs.

This article introduces a novel nested magnetic coupling mechanism characterized by a broad coupling area, high spatial magnetic field uniformity, and robust scalability, tailored to meet the scenario requirements of random load positions in UAV wireless power transfer. The mechanism ensures a continuous and reliable power supply to the load. Initially, electromagnetic field theory is employed to derive the 3-D spatial magnetic field strength within the coupling field area. A general expansion method for the nested magnetic coupling mechanism design is defined, integrating "cross-shaped" compensation coils to address the coupling blind spot issue. Subsequently, the system's optimal coupling boundary area is delineated from the perspective of power fluctuation, with the structural parameters of the magnetic coupling structure optimized to align with the design objectives of optimal coupling area and receiving power stability. Ultimately, an experimental testing platform for the UAV wireless power transfer system is constructed to substantiate that the proposed magnetic coupling mechanism maintains high stability of system output during movement.

II. ANALYSIS OF COUPLING MECHANISM OF NESTED MAGNETIC COUPLING MECHANISM

A. Determination of Nested Launch Module Structure

To meet the wide power supply requirements at random locations under load, this article proposes a nested power transmission module, as shown in Fig. 1. It consists of n square planar coils of different sizes with coincident geometric centers and a shield. The more nested coils there are, the larger the effective charging area covered by the system. This article studies the second-level nested module as an example, which is equipped with one lateral emission coil and an embedded emission coil, and explores the general construction method of n-level nested modules.

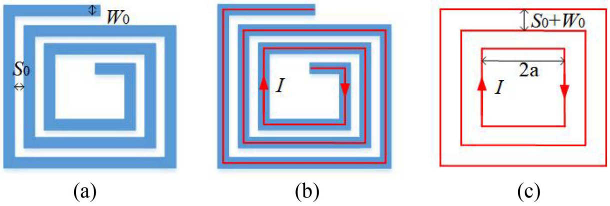

Fig. 2. Coil structure simplified schematic diagram.

For the second-level nested module, according to Faraday's law of electromagnetic induction, when the currents of the lateral emission coil and the embedded emission coil are in the opposite direction, the magnetic field directions inside the lateral emission coil and outside the embedded emission coil can overlap with each other. Then, a higher magnetic field intensity in the middle region can be generated. At the same time, the reverse magnetic field generated inside the embedded emission coil can lower the magnetic field curve at the corresponding position of the lateral emission coil, which makes the overall magnetic field intensity change in the coverage area of the transmitting coil tend to be flat, reduces the amplitude of mutual inductance change, and increases the effective charging area. The magnetic field is defined as being uniformly distributed if the magnetic flux density fluctuates by less than 5% within the specified area.

B. Calculation of Spatial Magnetic Induction Intensity for Nested Emission Modules

To facilitate calculation, the embedded coils, outer coils, and receiving coils are simplified, and it is assumed that the current flows uniformly in the coil, the geometric axis of the coil serves as the central line for the external effect of the current. The spiral axis in the coil can be equivalent to a concentric square structure, as shown in Fig. 2(a), where the coil turn spacing is denoted as S_0 and the Leitz wire diameter is denoted as W_0. The current flow inside the coil is shown in Fig. 2(b). The simplified geometric model of the coil is shown in Fig. 2(c), where the distance between the wires can be approximated as the sum of the coil diameter and the coil turn pitch, which is donated as $S_0 + W_0$.

Let the side length of the embedded coil, outer coil, and the innermost single-turn coil of the receiving coil be $2a$, $2b$, and $2c$, respectively. The side lengths of the remaining square coils can be expressed as follows:

$$2a_i = 2a + 2\left(i - 1\right)\left(W_0 + S_0\right) \tag{1}$$

$$2b_j = 2b + 2\left(j - 1\right)\left(W_0 + S_0\right) \tag{2}$$

$$2c_k = 2c + 2\left(k - 1\right)\left(W_0 + S_0\right). \tag{3}$$

Mathematical models are established for the ith embedded emission coil, jth lateral emission coil, and kth receiving coil,

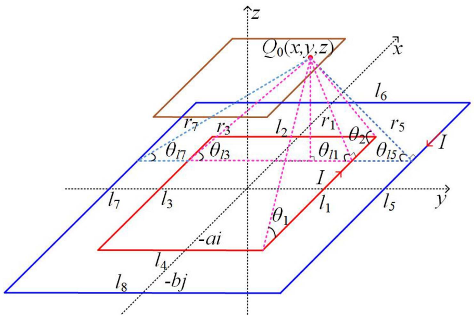

Fig. 3. Mathematical model of two-stage nested magnetic coupling mechanism.

as shown in Fig. 3. l_1 to l_8 represent the wire segments of the transmitting coils, respectively, and the currents in the embedded emission and lateral emission coils are denoted as I.

Point Q_0 represents an arbitrary point on the plane of the receiving coil, and the side lengths of the embedded and outer transmitting coils are $2a_\mathrm{i}$ and $2b_\mathrm{i}$, respectively.

According to Biot–Savart's law, the magnitude of the magnetic induction produced by a finite-length straight conductor at any point Q_0 in space can be obtained as

$$B = \frac{\mu_0}{4\pi}\int_{\theta_{m1}}^{\pi-\theta_{m2}} \frac{I\sin\theta}{r_m}d\theta = \frac{\mu_0 I}{4\pi r_m}\left(\cos\theta_{m1}+\cos\theta_{m2}\right). \tag{4}$$

Here, r_m is the distance from point Q_0 to the mth straight conductor, θ_{m1} and θ_{m2} are the angles between point Q_0 and the two ends of the mth conductor, and μ_0 is the permeability of vacuum. The analysis of the magnetic flux density distribution above point Q_0 on the y-axis is provided. Fig. 4 shows the cross-sectional views of the transmission module on the xoz and yoz planes, with the magnetic flux densities at point Q_0 for each side conductor already indicated.

Due to the parallel orientation of the plane of the receiving coil with the xy plane, only the z-component of the magnetic induction intersects the receiving coil. According to the superposition principle, the total magnetic induction in the z-axis direction at point Q_0 is

$$\begin{aligned}\boldsymbol{B}_z = \boldsymbol{B}_{l1-z} + \boldsymbol{B}_{l3-z} - \boldsymbol{B}_{l5-z} - \boldsymbol{B}_{l7-z} + \boldsymbol{B}_{l2-z} \\ + \boldsymbol{B}_{l4-z} - \boldsymbol{B}_{l6-z} - \boldsymbol{B}_{l8-z}.\end{aligned} \tag{5}$$

Substituting (4) into (5) for simplification, the magnetic induction intensity Bz in z-axis direction can be obtained as

$$B_\mathrm{z} = \frac{\mu_0 I}{2\pi}\begin{bmatrix} \frac{a_i-y}{(a_i-y)^2+z^2}\frac{a_i}{\sqrt{{a_i}^2+(a_i-y)^2+z^2}} \\ +\frac{a_i+y}{(a_i+y)^2+z^2}\frac{a_i}{\sqrt{{a_i}^2+(a_i+y)^2+z^2}} \\ -\frac{b_i-y}{(b_i-y)^2+z^2}\frac{b_i}{\sqrt{{b_i}^2+(b_i-y)^2+z^2}} \\ -\frac{b_i+y}{(b_i+y)^2+z^2}\frac{b_i}{\sqrt{{b_i}^2+(b_i+y)^2+z^2}} \end{bmatrix} + \frac{\mu_0 I}{2\pi}\begin{bmatrix} \frac{2a_i+x}{(a_i+x)^2+z^2}\left(\begin{array}{c}\frac{a_i+x-y}{\sqrt{(a_i+x)^2+(a_i+x-y)^2+z^2}} \\ \cdot\frac{a_i+x+y}{\sqrt{(a_i+x)^2+(a_i+x+y)^2+z^2}}\end{array}\right) \\ -\frac{2b_i}{{b_i}^2+z^2}\left(\frac{b_i-y}{\sqrt{{b_i}^2+(b_i-y)^2+z^2}}-\frac{b_i+y}{\sqrt{{b_i}^2+(b_i+y)^2+z^2}}\right)\end{bmatrix}. \tag{6}$$

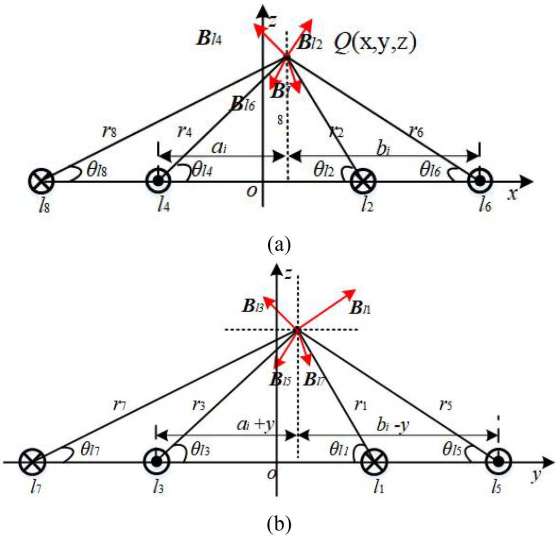

(a)

(b)

Fig. 4. Q_0 point magnetic induction intensity analysis diagram. (a) xoz section. (b) yoz section.

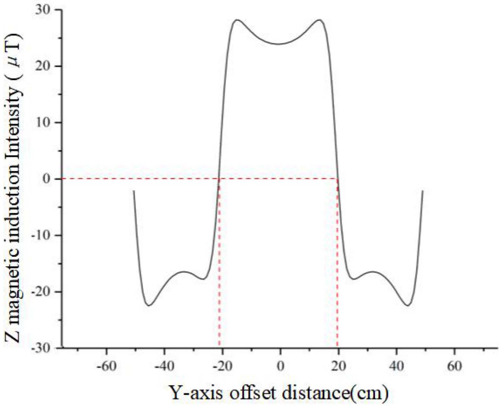

Fig. 5. Variation curve of z-axis magnetic induction intensity with moving distance at point Q_0.

C. "Cross-Shaped" Compensation Receiving Structure Design

The magnetic field distribution of the nested emission coil can be calculated by (6) shown at the bottom of this page. Let $a_\mathrm{i} =$ 200 mm, $b_\mathrm{i} =$ 500 mm, the distance z in the z-axis direction of the transmitting coil and the receiving coil equals 50 mm, $I =$ 10 A, $\mu_0 = 4\pi\times10^{-7}$Tm/A. The change curve of the magnetic induction intensity Bz with the movement distance along the y-axis is shown in Fig. 5.

According to Fig. 5, it can be seen that when the Y-offset distance is moved to −20 cm or 20 cm, the z-axis component

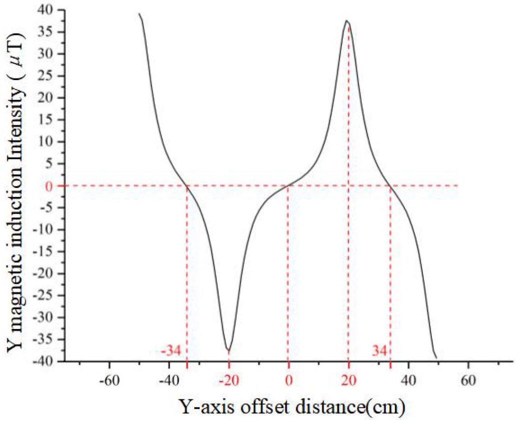

Fig. 6. Variation curve of y-axis magnetic induction intensity with offset distance at point Q_0.

of magnetic induction at Q_0 is zero and the magnetic induction cancels each other out at this point, which is the coupling blind spot. When the distance is within the range of [−20 cm, 20 cm], the magnetic induction is a positive value, and the numerical value of the magnetic induction fluctuates to a certain extent in most intervals. Therefore, it is necessary to design the size of the transmitting coil and the structure of the receiving coil reasonably to meet the requirements of uniform distribution of the magnetic field generated by the transmitting coil and stable distribution of the received power.

Further analysis is carried out on the magnetic induction intensity of point Q_0 in the x/y-axis direction. Due to the symmetry of the geometric structure, the variation law of the magnetic induction intensity in the x/y-axis direction at point Q_0 is the same. Therefore, only the y-axis direction is studied here. Since the wires l_2, l_4, l_6, and l_8 are parallel to the y-axis, there is no component in the y-axis direction at point Q_0. Therefore, the magnetic induction intensity in the y-axis direction at point Q_0 is provided by the wires l_1, l_3, l_5, and l_7, and the expression is

$$\begin{aligned}\boldsymbol{B}_y = \boldsymbol{B}_{l1} \cdot \sin\theta_{l1} + \boldsymbol{B}_{l7} \cdot \sin\theta_{l7} - \boldsymbol{B}_{l3} \cdot \sin\theta_{l3}\\ - \boldsymbol{B}_{l5} \cdot \sin\theta_{l5}. \qquad (7)\end{aligned}$$

The change curve is shown in Fig. 6. Since both transmitting coils are symmetric about the origin, the distribution of the magnetic field on both sides of the center point is of the same magnitude but opposite in direction. When y is in the range of [0, 50 cm], the magnetic induction intensity in the y-direction at point Q_0 shows an increasing trend followed by a decreasing trend. The magnetic induction intensity reaches its maximum at $y = 20$ cm when the magnetic fields superimpose each other.

Using finite element simulation software, spatial magnetic field analysis was conducted for B_z and B_y. The simulation results are shown in Fig. 7, and they are consistent with the theoretical analysis results.

According to the analysis of the spatial magnetic field mentioned above, when the receiving and transmitting coils are in a facing state, the magnetic induction intensity only intersects in the z-direction. When the component in the z-direction is zero, the magnetic induction intensity reaches its maximum in the x/y-directions. Therefore, the coupling effect of the planar receiving coil in a certain area can be compensated by coupling the x/y-directional magnetic fields with the compensation coil.

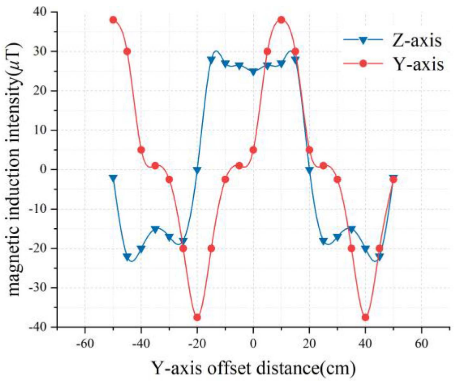

Fig. 7. Simulation curves of the variation of z-axis and y-axis magnetic induction with offset distance at point Q_0.

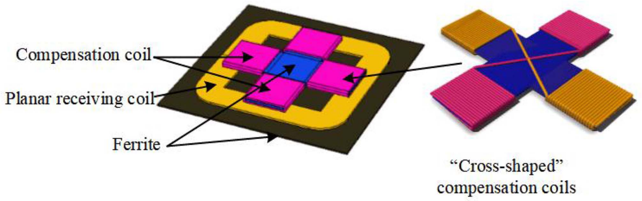

Fig. 8. "Cross-shaped" compensation receiving structure.

Based on the aforementioned circumstances, a "cross-shaped" compensation coil structure is proposed and integrated into the magnetic coupling mechanism to capture the magnetic flux density components along the x or y axes, thereby addressing the coupling blind spot issue. The overall receiving mechanism consists of two parts: 1) a planar receiving coil and 2) a "cross-shaped" compensation coil, as shown in Fig. 8. The planar receiving coil utilizes a planar square spiral coil structure that intersects with the longitudinal magnetic field. The compensation coil is composed of four-square spiral coils, with two compensation receiving coils on the same axis being wound in the same direction on a ferrite core with a single conductor, each intersecting with the magnetic field along the x and y axes, respectively. This design ensures academic and professional integrity.

D. Analysis of Magnetic Coupling Mechanism Circuit Model

The equivalent circuit model of the two-stage nested magnetic coupling mechanism is shown in Fig. 9. The transmitter side consists of two serially connected transmitting coils, and the receiver side consists of a planar receiving coil and a compensation coil connected in parallel. L_f is the compensating inductance on the transmitter side, $C_{\mathrm{s}1}$ and $C_{\mathrm{s}2}$ are the compensation capacitors on the transmitter side, and $C_{\mathrm{s}3}$, $C_{\mathrm{s}4}$, and $C_{\mathrm{s}5}$ are the compensation capacitors on the receiver side. The input voltage of the high-frequency ac power supply is V, L_1, and L_2 represent the external and embedded transmitting coils, respectively, L_3 represents the planar receiving coil, L_4 and L_5

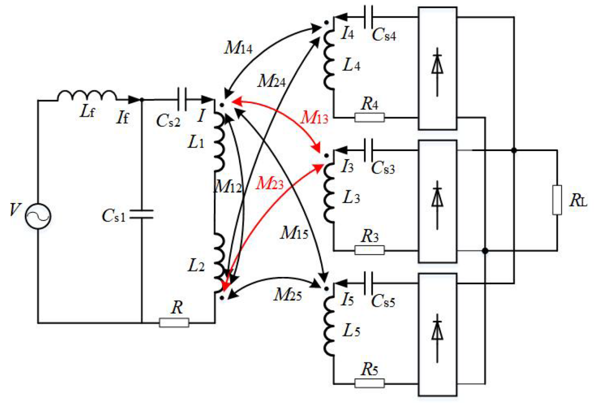

Fig. 9. System equivalent circuit diagram.

represent the compensation receiving coils parallel to the *x*-axis and *y*-axis, respectively, R is the total internal resistance of the transmitter coils, R_3–R_5 represent the internal resistances of the respective receiving coils, and R_L is the load. Since the three receiving coils are orthogonally positioned in space, the coupling degree between any two receiving coils is approximately zero. To simplify the calculations, the mutual inductance between the receiving coils is assumed to be zero.

To ensure efficient transmission, the system should reduce reactive power loss and meet the zero-phase angle operation.

The resonance conditions that the system should meet are

$$\begin{aligned}\omega &= \frac{1}{\sqrt{C_{\mathrm{S1}}L_\mathrm{f}}} = \frac{1}{\sqrt{C_{\mathrm{S2}}\left(L_1+L_2-2M_{12}-L_{\mathrm{f1}}\right)}}\\ &= \frac{1}{\sqrt{C_{\mathrm{S3}}L_3}} = \frac{1}{\sqrt{C_{\mathrm{S4}}L_4}} = \frac{1}{\sqrt{C_{\mathrm{S5}}L_5}}.\end{aligned} \tag{8}$$

Further calculations can be made for the output power of the transmitting side power supply P_in, the output power of the planar receiving coil on the load $P_{\text{out-z}}$, and the output power of the receiving compensation coil on the load $P_{\text{out-x}}$ and $P_{\text{out-y}}$, which are

$$P_\mathrm{in} = V^2\omega^2C_{s1}^2\left[R-\omega^2\left(\begin{array}{l}\frac{(M_{13}-M_{23})^2}{R_3+R_L}+\frac{(M_{14}-M_{24})^2}{R_4+R_L}\\ +\frac{(M_{15}-M_{25})^2}{R_5+R_L}\end{array}\right)\right] \tag{9}$$

$$P_{\text{out-z}} = I_3^2R_L = V^2C_{s1}^2\omega^4R_L\left(\frac{M_{13}-M_{23}}{R_3+R_L}\right)^2 \tag{10}$$

$$P_{\text{out-x}} = I_4^2R_L = V^2\omega^4C_{s1}^2R_L\left(\frac{M_{14}-M_{24}}{R_4+R_L}\right)^2 \tag{11}$$

$$P_{\text{out-y}} = I_5^2R_L = V^2\omega^4C_{s1}^2R_L\left(\frac{M_{15}-M_{25}}{R_5+R_L}\right)^2. \tag{12}$$

Fig. 10 shows the system output power and mutual inductance fluctuation curves at the receiver side when it is moved along the *x*-axis, *y*-axis, and diagonal directions. According to (10), (11), (12), and Fig. 10, it can be observed that there is a direct proportionality between mutual inductance and output power. Therefore, the output power curve for the *y*-axis direction movement is chosen for analysis.

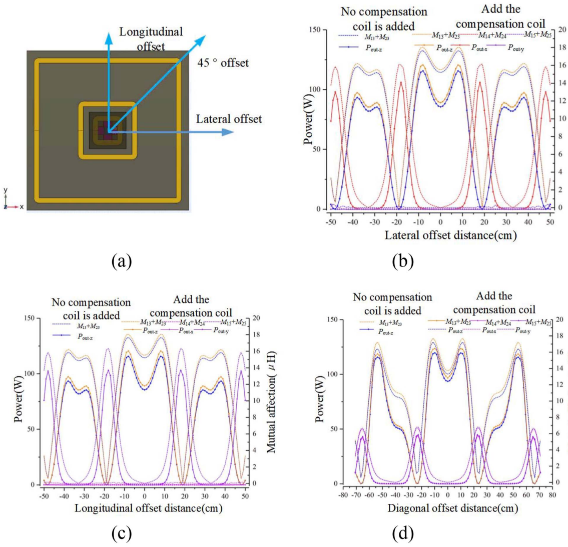

(a) (b)

(c) (d)

Fig. 10. Migration direction and power and mutual inductance change curve with migration distance. (a) Mobile diagram. (b) *X*-axis movemen. (c) *Y*-axis movement. (d) Diagonal movement.

When the receiver coil is located at the center position of the transmitter coil, the output power reaches a minimum value but can remain stable within a certain range. When the receiver coil is moved to the edge of the embedded transmitter coil, the output power of the planar receiver coil $P_{\text{out-z}}$, gradually decreases to zero, while the output power of the compensation coil $P_{\text{out-y}}$, increases to its maximum value. This validates the effectiveness of the "cross-shaped" compensation coil in eliminating coupling blind spots and enlarging the stable operating area of the system.

Based on the abovementioned analysis, it can be concluded that the variations in the output power and mutual inductance of the receiver coil are consistent with the theoretical analysis of the B_z variation trend. Moreover, the variations in the compensated receiver coil's port output power and mutual inductance are consistent with the theoretical analysis trend of B_y. This further demonstrates that the magnetic coupling mechanism proposed in this article can meet the system's operational requirements within a significant range of movement.

III. PERFORMANCE OPTIMIZATION METHOD FOR TWO-NESTED MAGNETIC COUPLING MECHANISM

A. Magnetic Coupling Stability Region Definition and Division Criteria

The equivalent circuit model of the magnetically coupled system is shown in Fig. 11. Since the system's transmission efficiency is a key parameter for evaluating the efficiency of wireless power transfer to a mobile load, it is necessary to solve for the effective magnetic coupling area to determine the high-efficiency power reception area for the mobile load, which can be obtained from the formula for the transmission efficiency of the magnetic coupling system

$$\eta = \frac{\omega^2{M_{1\mathrm{L}}}^2R_\mathrm{L}}{R_1(R_\mathrm{p}+R_\mathrm{L})^2+\omega^2{M_{1\mathrm{L}}}^2(R_\mathrm{p}+R_\mathrm{L})}. \tag{13}$$

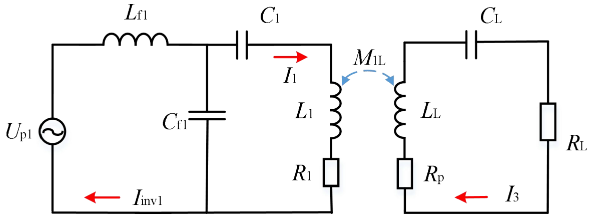

Fig. 11. Equivalent circuit of magnetic coupling system of square transceiver coil.

From (13), it can be seen that the transmission efficiency in a specific system is mainly related to the mutual inductance and load impedance. To achieve maximum transmission efficiency, the derivative of the load impedance R_{L} is taken to obtain the optimal state of load impedance matching. The system parameters must meet the conditions, as shown in

$$\frac{d\eta}{dR_L} = \frac{M_{1L}^2\omega^2 - M_{1L}^2\omega^2 R_L\left(2R_1\left(R_p+R_L\right)\right)}{\left(R_1(R_p+R_L)^2 + M_{1L}^2\omega^2\left(R_p+R_L\right)\right)^2}. \tag{14}$$

To solving for the optimal load matching condition, set (14) equal to 0, and the result, as shown in (15). When the load meets this condition, the system can operate at maximum efficiency

$$R_L = R_p\sqrt{1+\omega^2 M_{1L}^2/(R_1R_p)}. \tag{15}$$

From (15), it is evident that the optimal load value for efficient dynamic wireless power transfer to a mobile load is primarily related to $\omega^2 M_{1\mathrm{L}}{}^2/R_1R_{\mathrm{p}}$, which is defined as the load matching factor and represented by the symbol ξ. By substituting (15) into (13), the expression for the system's transmission efficiency under optimal load conditions can be obtained

$$\eta = \frac{\xi}{2(1+\xi)^{1/2}+\xi+2}. \tag{16}$$

From (16), it can be inferred that under optimal load conditions, the transmission efficiency is solely dependent on the load matching factor ξ. Provided that the quality factors of the transmitter and receiver coils remain constant, the variation of the load matching factor during the movement of the mobile load is primarily determined by the coupling coefficient. Since the coupling coefficient $k_{1\mathrm{L}}$ varies in real-time with the movement of the mobile load, it causes fluctuations in the optimal load value, thereby preventing the system from stably operating at the point of maximum efficiency. The load matching factor ξ is expressed in terms of the coupling coefficient $k_{1\mathrm{L}}$, the quality factor of the transmitter coil Q_1, and the quality factor of the receiver coil Q_{L}, as shown in

$$\xi = k_{1L}^2 Q_1 Q_L. \tag{17}$$

Using MATLAB software to analyze the relationship between transmission efficiency and the load matching factor ξ in (16) is depicted in Fig. 2. The results indicate that when the load matching factor ξ is less than 200, the transmission efficiency is relatively low and decays rapidly. When ξ exceeds 200, the transmission efficiency is greater than 85% and changes more slowly, with minor fluctuations having a smaller impact on the transmission efficiency.

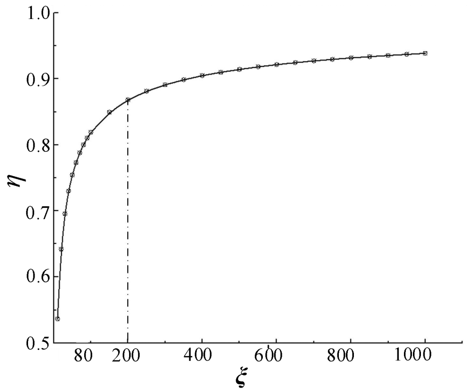

Fig. 12. Relation curve between load matching factor and transmission efficiency.

Using the coupling coefficient at the transmitter and receiver ends expressed by mutual inductance and self-inductance of the coils, and through (17), the ratio of the load matching factor before and after the movement of the receiver coil can be obtained

$$\frac{\xi'}{\xi} = \frac{k_{1\mathrm{L}}'^2}{k_{1L}^2} = \frac{M_{1\mathrm{L}}'^2}{M_{1L}^2}. \tag{18}$$

In (18), it is assumed that the load matching factors before and after the movement of the receiver coil, as well as the mutual inductance and coupling coefficients of the magnetic coupling system, are represented as ξ and ξ', $M_{1\mathrm{L}}{}^2$ and $M'_{1\mathrm{L}}{}^2$, and $k_{1\mathrm{L}}{}^2$ and $k'_{1\mathrm{L}}{}^2$, respectively.

From (18), it can be deduced that the fluctuation of the load matching factor can be characterized by the rate of change of the mutual inductance in the magnetic coupling system. Combined with the results shown in Fig. 12, when the load matching factor ξ is greater than 200, even with minor fluctuations, a high transmission efficiency can be achieved. Therefore, under the condition that the transmitter and receiver coils have high quality factors, by limiting the fluctuation range of the mutual inductance parameters, efficient power reception during the movement of the mobile load can be realized.

Based on the aforementioned theoretical analysis, the time-varying mutual inductance is used as a parameter to delineate the effective magnetic coupling area. Let the mutual inductance value when the axes of the transmitter and receiver coils coincide be the standard value M_{saver}. Considering the system's good output power stability and resistance to offset, the fluctuation range of the time-varying mutual inductance deviating from the standard value by ±25% is set, i.e., the normalized mutual inductance values of 0.75 and 1.25 are taken as the lower and upper boundaries of the effective magnetic coupling area. The area enclosed by these boundaries is the effective magnetic coupling area at that transmission distance. When the receiver coil continues to deviate from the origin, and the deviation of the mutual inductance value exceeds the set upper and lower boundaries, it will no longer meet the requirements for efficient

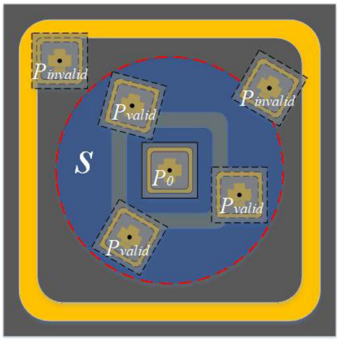

Fig. 13. Diagram of optimal coupling region.

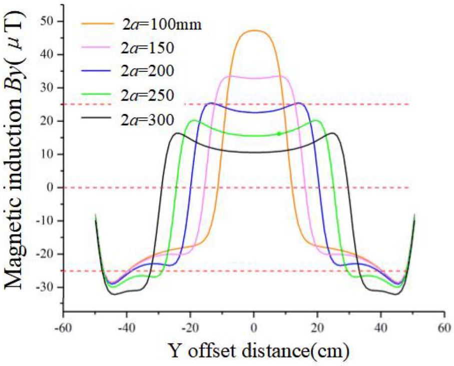

Fig. 14. Variation of magnetic induction intensity with offset distance.

wireless power reception of the mobile load. This area is referred to as the ineffective magnetic coupling area.

B. Coupling Performance Evaluation Method

During the operation of the system, the output power at the receiver end is required to meet the amplitude and stability requirements. Typically, the center of the rectangular coil is the maximum received power. In the system designed in this article, the value of the central region of the emission coil is relatively low due to the inverse compensation effect of the embedded emission coil. Based on this, the received power P_{base} at the position where the geometric centers of the transmitting and receiving coils coincide is taken as the reference value. It is further defined that the set of all positions of the receiver coil, projected within the plane of the transmitting module, which have power fluctuations of less than 25% when the receiver coil moves in any direction, is referred to as the optimal coupling region. We define the stable operating region as the output power fluctuation range less than 25%, as shown in Fig. 13. Assuming the circular blue region S represents the optimal coupling region, P_{valid} represents the power value of the receiver coil within the optimal coupling region, and P_{invalid} represents the power value when the receiver coil moves outside the optimal coupling region. According to the specified conditions, the power value P_{valid} for stable operation of the load should satisfy the following equation in relation to the reference value P_{base}:

$$0.75P_{\text{base}} \leq P_{\text{valid}} \leq 1.25P_{\text{base}}. \tag{19}$$

C. Optimization of Physical Parameters of Nested Launch Module

The physical parameters of the outer transmitting coil in a nested transmitter module structure primarily depend on the specific application requirements for the power supply area. However, the design of the receiver coil parameters is usually strictly limited by the type of load. In the following example, we will discuss the optimization design of the parameters for a two-level nested transmitter module and explore general methods for the design of parameters for multi-level nested transmitter modules.

Assuming the dimensions of the outer transmitting coil are 1000×1000 mm^2 and the dimensions of the planar receiver coil are 200×200 mm^2, we will vary the value of the edge length ($2a$) of the embedded transmitting coil and analyze the magnetic induction intensity variation of point Q_0 along the z-axis for different values.

As shown in Fig. 14, as the size of the embedded transmitting coil increases, the magnetic induction intensity in the central region gradually decreases, and the depth of the depression at the center point increases. However, the overall value of the magnetic induction intensity in the edge region gradually increases. To ensure a stable distribution of the magnetic field in the region above the transmitter module, it is desirable to maximize the size of the embedded transmitting coil while ensuring that the mean values of the magnetic induction intensity in the regions on both sides of the coupling blind spot are similar. In Fig. 14(b), the overall mean value of the magnetic induction intensity in the edge region is maintained at around 25 μH, and the corresponding range of values for the size of the embedded transmitting coil in the [150 mm, 200 mm]

Assuming the receiver coil has a side length of 200 mm, the outer transmitting coil has a side length of 1000 mm, the coupling distance is 50 mm, the amplitude of the ac input voltage is 50 V, and the resonant frequency is 85 kHz. The initial value of the edge length of the embedded transmitting coil is 300 mm, and it gradually increases in steps of 10 mm during the variation process, while keeping the number of turns and turn spacing of the coil constant. Based on the above method, we explore the output power and the area of the optimal magnetic coupling region during the movement of the receiver coil in different directions, and further determine the size of the embedded transmitting coil.

Fig. 15 shows the mapping relationship between different physical sizes of the embedded coil and the received power. From the results, it can be observed that as the size of the embedded transmitting coil increases, the overall power distribution in both the central and peripheral regions of the embedded transmitter module gradually approaches each other. However, at the same time, the fluctuation of power in the geometric center region also increases. Further analysis is needed to determine the requirements for power fluctuation limitations.

The maximum fluctuation rate of the received power in the central region can be calculated. According to the definition of the optimal coupling region, the following relationship is

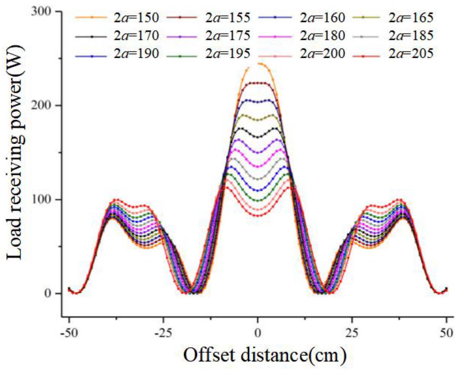

Fig. 15. Change of load receiving power under different embedded coil sizes.

TABLE I
λ_1, λ_2, AND D VALUES UNDER DIFFERENT EMBEDDED COIL SIZES

$2a$/mm	λ_1	λ_2	D/mm
300	0	67.54%	125.8
310	0	63.93%	139.6
320	1.01%	59.82%	147.4
330	2.89%	54.84%	165.8
340	5.56%	45.03%	179.8
350	8.27%	42.27%	197.4
360	11.42%	34.55%	204.2
370	14.88%	25.57%	242.0
380	17.19%	15.64%	273.0
390	20.67%	4.12%	549.4
400	23.15%	9.23%	586.8
410	26.20%	20.00%	574.0

obtained:

$$\begin{cases} \lambda_1 = \frac{|P_{\max 1} - P_{\text{baseline}}|}{P_{\text{baseline}}}, \lambda_2 = \frac{|P_{\text{baseline}} - P_{\max 2}|}{P_{\text{baseline}}} \\ \lambda_1 \leq 0.25, \lambda_2 \leq 0.25 \end{cases}. \tag{20}$$

λ_1 and λ_2 represent the power fluctuation rates in the central and edge regions, respectively, while $P_{\max1}$ and $P_{\max2}$ represent the maximum received power in the central and edge regions, respectively. Besides, D is defined as the radius of the movement region that satisfies the power requirement in (20). Table I presents the values of key parameters for different sizes of the embedded coil.

By observing the data in the table, it can be seen that when the value of $2a$ is within the range [380 mm, 400 mm], the power fluctuation rates in the central and edge regions of the system satisfy the power fluctuation range defined by the optimal coupling region. Taking the value of $2a$ as 400 mm, the maximum power fluctuation rates in the central and edge regions of the system are 23.15%, which meets the design requirements mentioned earlier. The corresponding effective movement distance D is at its maximum value of 586.8 mm, with the embedded transmitting coil size being 400 × 400 mm^2.

By observing the data in the table, it can be seen that when the value of $2a$ is within the range [380 mm, 400 mm], the power fluctuation rates in the central and edge regions of the system satisfy the power fluctuation range defined by the optimal coupling region. Taking the value of $2a$ as 400 mm, the maximum power fluctuation rates in the central and edge regions of the system are 23.15%, which meets the design requirements mentioned earlier. The corresponding effective movement distance D is at its maximum value of 586.8 mm, with the embedded transmitting coil size being 400 × 400 mm^2.

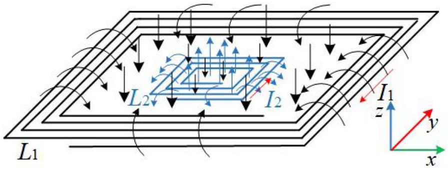

Fig. 16. Nested emission module magnetic field direction.

D. Analysis of Cross-Shaped Coupling Effects Between Coils

A nested wireless power transfer module is composed of multiple square planar coils of different sizes, with their geometric centers aligned along the same axis. When an alternating current is applied to any of the coils, the generated magnetic field will intersect with another coil, resulting in cross-coupling between the coils and affecting the coupling efficiency between the transmitter and receiver coils.

Fig. 16 illustrates the flow of the spatial magnetic field generated by the nested transmitter module. L_1 and L_2 represent the two transmitter coils, while I_1 and I_2 represent the currents flowing through them. The magnetic flux passing through any transmitter coil should be the sum of its self-inductance flux and mutual inductance flux. Assuming that the magnetic flux passing through the regions occupied by transmitter coils 1 and 2 are Ψ_1 and Ψ_2, respectively, the following equations can be derived

$$\begin{cases} \psi_1 = L_1 I_1 - M_{12} I_2 \\ \psi_2 = L_2 I_2 - M_{12} I_1 \end{cases}. \tag{21}$$

From (21), M_{12} represents the mutual inductance between two transmitting coils. The equivalent self-inductance after considering cross coupling between coils is

$$\begin{cases} L_1' = \frac{\psi_1}{I_1} \\ L_2' = \frac{\psi_2}{I_2} \end{cases}. \tag{22}$$

According to (21) and (22), it can be seen that when there is mutual inductance between two transmitting coils with opposite current phases, the magnetic flux passing through the circuit where the coils are located will decrease, thereby reducing the equivalent self-inductance value of the coils.

Fig. 17 shows the distribution of transferred power and efficiency before and after considering cross-coupling in the system. It can be observed from the Fig. 17 that the overall efficiency of the system significantly improves when cross-coupling is taken into account, while the transferred power remains almost unchanged. The cross-coupling between the transmitter coil units affects the equivalent self-inductance of adjacent coils, which makes traditional high-order compensation topology parameter design methods unable to operate the system at the resonant state. Additionally, cross-coupling between coil units generates reactive circulating currents, leading to a decrease in the overall efficiency of the system. Furthermore, the *LCC*-S high-order resonant compensation network can maintain a constant current characteristic for the transmitter coil, allowing the system

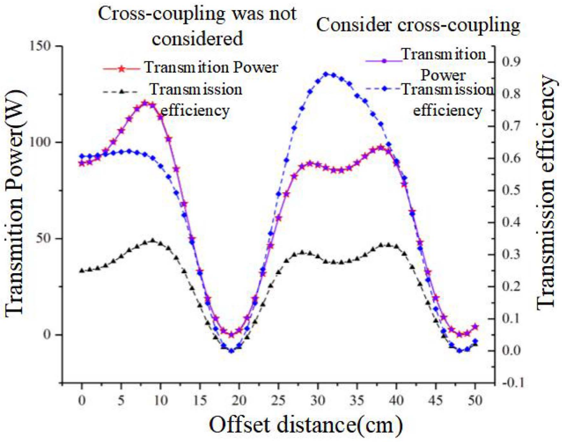

Fig. 17. System power and efficiency distribution before and after the considering cross-shaped coupling.

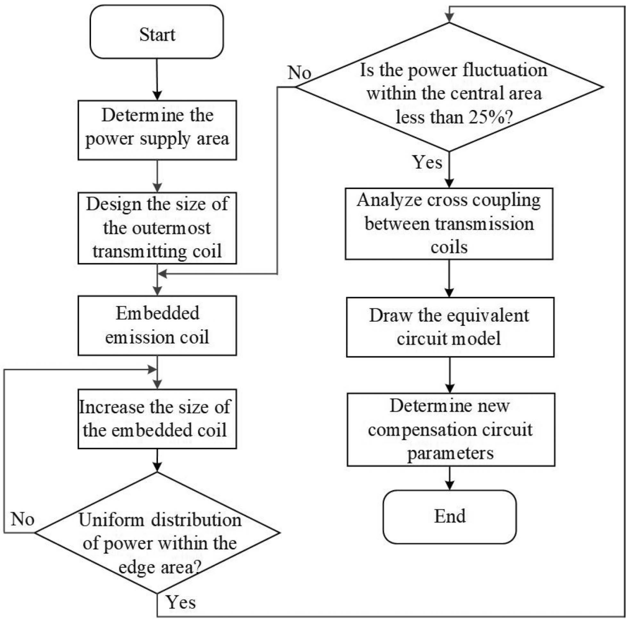

Fig. 18. Stable expansion method of nested transmitting module.

output power to be unaffected by cross-coupling. Therefore, the compensation parameters of the two transmitter coils need to be optimized to achieve decoupling and maintain a higher transmission efficiency for the system.

E. General Expansion Methods for Nested Launch Module Design

In the design of multilevel nested transmission modules, the specific number of nested coils is directly related to the size of the power supply area, which is determined by the specific operating scenario of the load [28]. The design method should possess generality and scalability, which is called the table expansion method of bested transmitting module in this article. Fig. 18 presents a general method for stable expansion of multilevel nested transmission modules, which consists of three steps as follows.

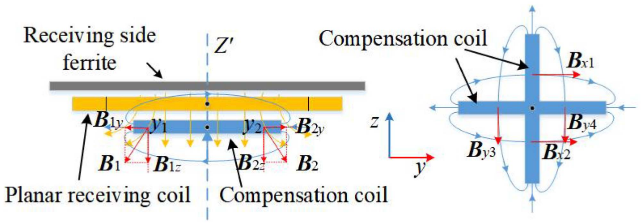

(a) (b)

Fig. 19. Receiver coil magnetic field distribution. (a) *yoz*-Schematic diagram. (b) *xoy*-Schematic diagram.

Step 1: Determine the dimensions of the outermost transmitting coil. The size of the outermost transmitting coil should match the size of the system's power supply area. Based on the required power level of the system, the physical parameters of the coils are designed progressively from the outermost to the innermost coil.

Step 2: Optimize the dimensions of the nested coils. By taking advantage of the weakening effect of the magnetic field in the central area and the strengthening effect in the edge area of the two coils with opposite current phases, the transmitting coils are nested progressively. The magnetic induction intensity gradually increases from the edge area to the central area, and the physical parameters of each nested coil level are optimized to ensure that the overall magnetic field induction intensity fluctuates within a specified range.

Step 3: Decoupling design between transmitting coils. In order to achieve efficient transmission in the system, the resonant conditions of the compensation topology for the transmitting end are rederived based on the equivalent circuit model of cross-coupling between transmitting coils. The compensation circuit parameters are optimized to achieve decoupling between the transmitting coils.

IV. OPTIMIZATION OF RECEIVING COIL STRUCTURE

A. Analysis of the Influence of Cross-Shaped Compensation Coils on Coupling Performance

The "cross-shaped" compensation coil solves the issue of blind spots by coupling the magnetic fields in the *x*- and *y*-directions. However, due to the different cross-coupling effects between the compensation coil and the planar receiving coil, it is necessary to analyze the impact of the "cross-shaped" compensation coil on the coupling performance of the system.

The planar receiving coil and the compensation receiving coil are spatially orthogonal, so the main magnetic flux generated by each coil does not intersect with the other receiving coils. Fig. 19(a) illustrates the magnetic field distribution in the *yoz* plane between the receiving coil and the *y*-axis compensation coil. Here, *Z*' is the geometric axis of the planar receiving coil, y_1 and y_2 are two points symmetrically positioned on the compensation receiving coil with respect to the geometric axis. The planar receiving coil produces a *y*-axis magnetic field at y_1 and y_2, with equal magnitudes but opposite directions, given by

$$\boldsymbol{B}_{y1}+\boldsymbol{B}_{y2}=0. \tag{23}$$

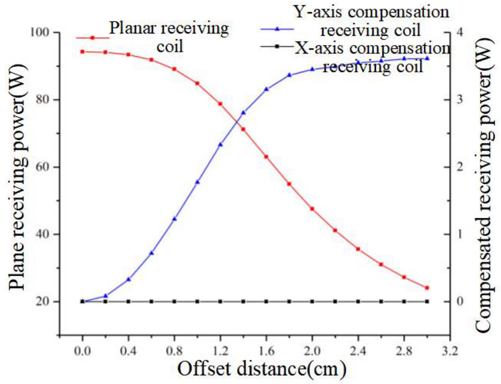

Fig. 20. Curve of the power of coil at the receiving end with the offset distance.

Since the compensation coil coincides with the geometric center of the planar receiving coil and is symmetric with respect to the geometric axis, the sum of the *y*-axis magnetic fields generated by the planar receiving coil in the region where the compensation coil is located is zero. Therefore, the planar receiving coil does not affect the compensation coil. Due to the structural symmetry, the total magnetic flux passing through the compensation coil by the receiving coil is almost zero, which means there is no cross-coupling between the two coils. Similarly, analyzing Fig. 19(b), we can observe that the geometric centers of the two coils coincide and are perpendicular to each other, resulting in almost zero magnetic field intersecting between the two coils.

To verify the correctness of the above analysis, we take the receiving coil and the *y*-axis compensation coil as an example. The receiving coil is positioned above the geometric center of the transmitting end, and the position of the planar receiving coil is fixed. The “cross-shaped” receiving compensation coil is gradually moved along the *y*-axis to analyze the distribution characteristics of the received power.

The change in received power with the distance of movement is analyzed, as shown in Fig. 20. It can be observed that as the distance of movement increases, the power of the receiving coil gradually decreases, while the power of the *y*-axis compensation coil gradually increases. The power value of the *x*-axis compensation coil remains zero. Therefore, when the *y*-axis compensation coil moves, the total magnetic flux within the planar receiving region is no longer zero. Its influence due to cross-coupling increases with the increase in the distance of movement, resulting in a gradual decrease in the received power of the planar receiving coil. On the other hand, the *x*-axis compensation receiving coil remains symmetric about the *Z*’-axis. The sum of the magnetic fields in the *x*-axis component within the region does not contribute to cross-coupling with the planar receiving coil.

In summary, to prevent the effects of cross-coupling between the receiving coil and the compensation coil, it is necessary to ensure symmetry of the compensation coil with respect to the geometric center axis of the receiving coil. Additionally, considering the structural characteristics of the compensation coil itself, the geometric center of the “cross-shaped” compensation coil should coincide with the geometric center of the planar receiving coil.

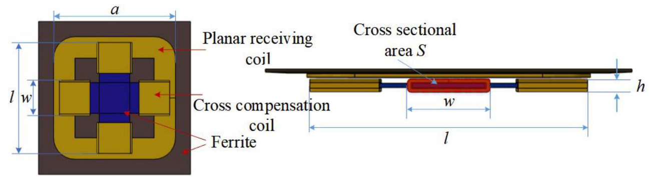

(a) (b)

Fig. 21. Receiver coil diagram. (a) Vertical view. (b) Side view.

B. *Optimization of Structural Parameters for the “Cross-Shaped” Receiving Compensation Coil*

When the circuit parameters and coil structure on the transmitting side are fixed, the received power of the compensation coil is mainly influenced by its own parameters. As shown in Fig. 21, the spatial structure of the receiving coil is a square planar coil with a side length of 200 mm. In the Fig. 21, *w* represents the width of a single compensation coil, *l* represents the length of the compensation coil, *h* represents the thickness of the compensation coil, and *S* represents the cross-sectional area of the compensation coil.

According to Faraday’s law of electromagnetic induction

$$E = -n\frac{d\Phi}{dt} \tag{24}$$

$$\Phi = \iint_S B \cdot ds = \int_S B_{p-y} \cdot dxdz \tag{25}$$

where Φ represents the magnetic flux generated by the transmitting module within the compensation coil, n is the number of turns of the coil, and E is the induced electromotive force at the two ends of the coil. From (24) and (25), we can see that the induced electromotive force E is positively correlated with the number of turns of the coil and the cross-sectional area S of the coil. Furthermore, the receiving coil should be miniaturized and lightweight as much as possible, with a fixed thickness of the ferrite material used for matching the compensation coil set to 3 mm. The compensation coil should be tightly wound to ensure that the thickness h remains constant, and its length should not exceed the length of the receiving coil. The cross-sectional area S of the coil is mainly determined by the width w of the compensation coil, while the number of turns of the coil is mainly determined by the length l of the compensation coil. By changing the values of the parameters w and l, the distribution of power in the compensation coil under different structural parameters can be investigated.

Figs. 20 and 22 show the variation curves of the received power at the receiving end with the movement distance under different lengths and widths of the compensation coil. It can be seen that the received power of the “cross-shaped” compensation coil first increases and then decreases, with the extreme point occurs near a travel distance of 200 mm. The overall power distribution is basically consistent with the analysis results of the magnetic induction intensity in the *y*-axis direction in Fig. 6. Additionally, the power of the “cross-shaped” compensation

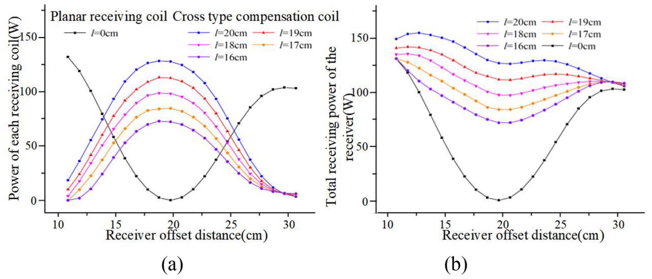

Fig. 22. Received power distribution under different compensation coil lengths. (a) Power of each coil. (b) Total power.

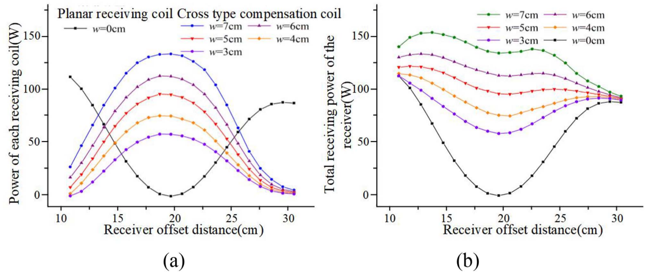

Fig. 23. Received power distribution under different compensation coil widths. (a) Power of each coil. (b) Total power.

coil complements the received power without the compensation coil, proving that the "cross-shaped" compensation coil can effectively solve the blind spot coupling problem. Furthermore, Fig. 22(b) shows that the overall power of the compensation receiving coil increases with the length of the coil. When the length of the compensation coil is 190 mm, the overall power fluctuates the least and satisfies the optimal power fluctuation range in the coupling area. Therefore, a compensation coil length of 190 mm is chosen, and the compensation coil width is optimized based on this. Fig. 23(b) shows the overall received power variation curve with the movement of the receiving end when the compensation coil length is 190 mm and the width varies. It is evident that as the width of the compensation coil increases, the level of indentation in the received power within the [10, 30] cm movement range gradually decreases. When the width of the compensation coil is 50 mm, the overall power meets the definition of the optimal coupling area. Hence, it is determined that the length (l) of the compensation coil is 190 mm, the width (w) is 50 mm, and the thickness (h) is 8 mm.

V. EXPERIMENTAL STUDY

A. *Nested UAVs Wireless Power Supply Experimental Platform*

The experimental platform for the nested UAVs wireless power transfer system is set up, as shown in Fig. 24. The outer coil has a side length of 1000 mm, while the inner embedded coil has a side length of 400 mm. Both coils are wound with a single strand of Litz wire, consisting of 10 turns. The Litz wire used has a diameter of 2.5 mm, and the spacing between turns is 1 mm. The receiving coil has a side length of 200 mm, and the compensation coil is tightly wound around the "cross-shaped" ferrite core, with 40 turns. The relative permeability μ_r of the ferrite is 3300. The receiving coil and the compensation coil are placed in a position where their geometric centers align, as shown in Fig. 25(b).

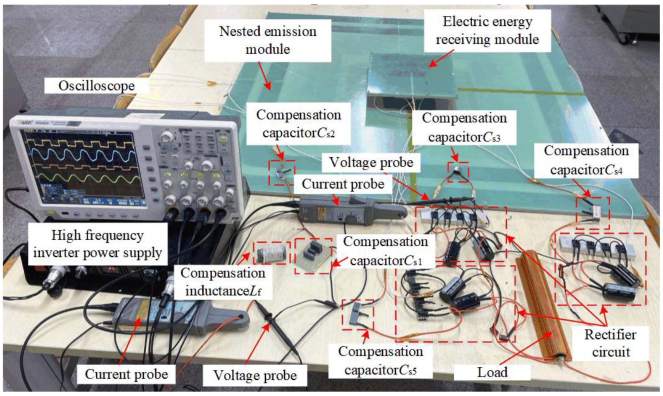

Fig. 24. Experimental platform of nested UAVs wireless power supply system.

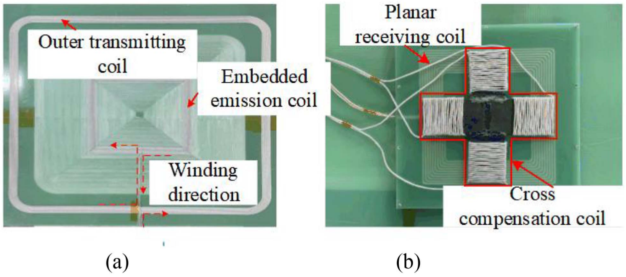

(a) (b)

Fig. 25. Coupling coil winding physical diagram. (a) Transmitting coil. (b) Receiving coil.

TABLE II
COUPLING COIL PARAMETERS

Coil parameters	L_1/μH	R/Ω	C/nF
Outer transmitting coil	486.68	0.32	5.80
Embedded transmitting coil	158.05	0.19	5.80
Flat receiving coil	84.88	0.14	41.31
Lateral compensation coil	185.05	0.17	18.95
Longitudinal compensation coil	183.43	0.17	19.11

The experimental parameters are set to be consistent with the simulation parameters. However, due to the manual winding of the coupling coils, there are some differences in self-inductance compared to the simulation parameters. Therefore, further matching of resonance parameters is needed. The parameters of the coupling mechanism in the experiment are shown in Table II. Fig. 26 shows the waveforms of the input voltage V_{in}, input current I_{f}, rectified input voltage V_{out}, and current I_4 at the geometric center position as well as at the blind spot of coupling. It can be observed from Fig. 26 that the phase angles of the input and output voltage and current are close to 0, indicating that the system is operating in a resonant state.

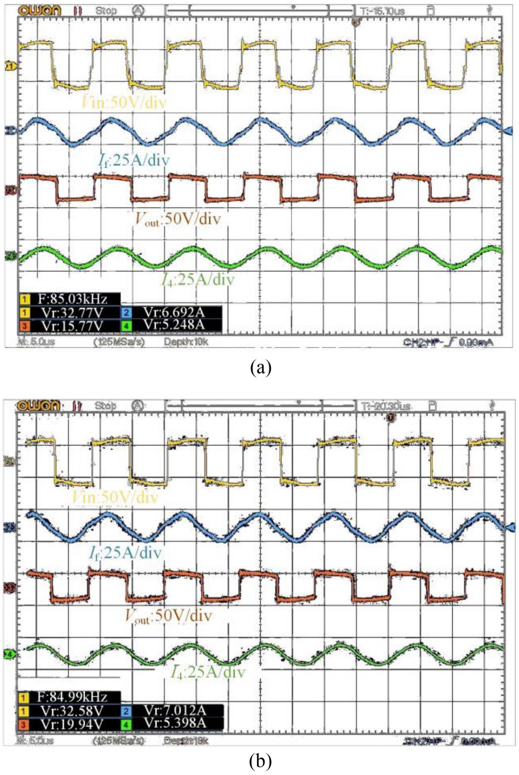

(a)

(b)

Fig. 26. System input and output waveform. (a) At the geometric center point. (b) At the coupling blind spot position.

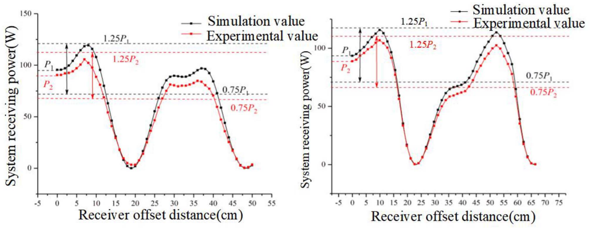

(a) (b)

Fig. 27. Variation diagram of surface receiving coil power with offset distance. (a) Lateral movement. (b) Diagonal movement.

B. Nested Launch Module Power Supply Area Testing

By keeping the position of the transmission module fixed, the receiving end is moved along the horizontal and diagonal directions from the geometric center point, with movement distances of 500 mm and 500 mm, respectively. The experimental results are shown in Fig. 27.

Fig. 27 shows the power fluctuation curves of the planar receiving coil at different movement distances. P_1 and P_2 represent the simulated and experimental results of the received power when the receiving end is at the geometric center point of the transmitting coil. It can be observed that both the central area and the edge area above the transmission module meet the requirements of the optimal coupling area. The errors in the effective horizontal and diagonal movement distances compared to the experimental values are 8.6% and 3.2%, respectively. The change trend of the received power at the receiving end is consistent with the simulation results, demonstrating that the embedding method of the transmission coil can expand the power supply area of the system.

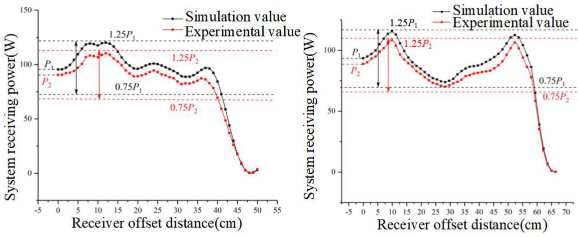

(a) (b)

Fig. 28. Variation of received power with offset distance after adding compensation coil. (a) Lateral movement. (b) Diagonal movement.

C. Experimental Testing of the Effect of the "Cross-Shaped" Compensation Coil

To validate the effectiveness of the "cross-shaped" compensation coil in addressing the blind spot coupling issue, a spatial structure with a square planar coil nested inside a "cross-shaped" compensation coil is used at the receiving end. The position of the transmission module remains fixed, while the receiving end is moved along the horizontal and diagonal directions from the geometric center point. The experimental results are shown in Fig. 28.

The power fluctuation curves of the receiving end with the addition of the compensation coil at different movement distances are analyzed, as depicted in Fig. 28. It can be observed that the power dip at the receiving end is significantly improved with the addition of the compensation coil. The fluctuation amplitude of the load power is relatively small throughout the entire movement process, and the power values meet the requirements of the optimal coupling area. The experimental test yields an effective horizontal movement distance of 402.4 mm, with an error of 2% compared to the simulation results. The effective diagonal movement distance is 586.3 mm, with an error of 1% compared to the simulation results. The results demonstrate that the planar "cross-shaped" compensation coil effectively solves the blind spot coupling issue at the transmitting and receiving ends.

VI. CONCLUSION

In this study, we have conducted research on the magnetic coupling mechanism of UAVs wireless power transfer systems to meet the demand for power supply to loads in a wide range of randomly positioned locations. We proposed a nested UAVs wireless power transfer system. First, we established a mathematical model for the nested magnetic coupling mechanism. By applying electromagnetic field theory, we obtained the magnetic field distribution characteristics in the space above the nested transmission module, and based on these characteristics, we proposed the "cross-shaped" compensation receiving coil to eliminate the coupling blind spots in the system. Second, we proposed an evaluation method for the optimal coupling area and used it as the basis for optimizing the parameters of the nested transmission coil and "cross-shaped" compensation receiving coil. Finally, an experimental platform for the nested UAVs wireless power transfer system was built, and the effectiveness of the nested transmission module's power supply area and the "cross-shaped" compensation receiving coil in addressing the blind spot coupling issue was verified through experiments involving the movement of the receiving end. The results showed that the nested magnetic coupling mechanism can provide a large range of stable and reliable power supply area, meeting the power supply requirements of moving loads over a large area.

REFERENCES

[1] M. Xue, Q. Yang, P. Zhang, J. Guo, Y. Li, and X. Zhang, "Application status and key issues of wireless power transmission technology," *Trans. China Electrotechnical Soc.*, vol. 36, no. 8, pp. 1547–1568, 2021.

[2] Z. Yuan et al., "A power-enhancing complementary coupling integration strategy for misalignment-tolerant WPT systems," *IEEE Trans. Power Electron.*, vol. 38, no. 11, pp. 14689–14701, Nov. 2023.

[3] S. Wu, X. Chen, X. Meng, C. Cai, W. Cai, and S. Yang, "Electric-field coupled wireless power transfer system with misalignment-tolerance and light-weight characteristics for unmanned aerial vehicle applications," *Proc. Chin. Soc. Elect. Eng.*, vol. 43, no. 6, pp. 2404–2412, 2023.

[4] R. Hasaba, K. Okamoto, S. Kawata, K. Eguchi, and Y. Koyanagi, "Magnetic resonance wireless power transfer over 10 m with multiple coils immersed in seawater," *IEEE Trans. Microw. Theory Techn.*, vol. 67, no. 11, pp. 4505–4513, Nov. 2019.

[5] J. Jia and X. Yan, "Research tends of magnetic coupling resonant wireless power transfer characteristics," *Trans. China Electrotechnical Soc.*, vol. 35, no. 20, pp. 4217–4231, 2020.

[6] S. Ruddell, U. K. Madawala, and D. J. Thrimawithana, "A wireless EV charging topology with integrated energy storage," *IEEE Trans. Power Electron.*, vol. 35, no. 9, pp. 8965–8972, Sep. 2020.

[7] Z. Yuan, M. Saeedifard, C. Cai, Q. Yang, P. Zhang, and H. Lin, "A misalignment tolerant design for a dual-coupled LCC-S-compensated WPT system with load-independent CC output," *IEEE Trans. Power Electron.*, vol. 37, no. 6, pp. 7480–7492, Jun. 2022.

[8] Z. Guan and B. Zhang, "Development and application of wireless power transfer technology for industrial movable robot," *Guangdong Electric Power*, vol. 32, no. 8, pp. 24–34, 2019.

[9] H. Matsumoto, Y. Shibako, and Y. Neba, "Contactless power transfer system for AGVs," *IEEE Trans. Ind. Electron.*, vol. 65, no. 1, pp. 251–260, Jan. 2018.

[10] M. Z. Chaari and R. Al-Rahimi, "The impact of wireless power charging on the future of the battlefield," in *Proc. Int. Wireless Commun. Mobile Comput.*, 2021, pp. 1563–1568.

[11] H. M. Harshitha, S. Sureshkumar, S. S. A, S. I. Zabiulla, and R. R. Kumar, "Wireless power transfer to charge low power device," in *Proc. Int. Conf. Des. Innovations 3Cs Compute Communicate Control*, 2021, pp. 61–64.

[12] J. Chen, R. Ghannam, M. Imran, and H. Heidari, "Wireless power transfer for 3D printed unmanned aerial vehicle (UAV) systems," in *Proc. IEEE Asia Pacific Conf. Postgraduate Res. Microelectronics Electron.*, 2018, pp. 72–76.

[13] U. Gordhan and S. Jayalath, "Wireless power transfer system for an unmanned aerial vehicle," in *Proc. 12th Power Electron., Drive Syst., Technol. Conf.*, 2021, pp. 1–5.

[14] A. M. Jawad, H. M. Jawad, R. Nordin, S. K. Gharghan, N. F. Abdullah, and M. J. Abu-Alshaeer, "Wireless power transfer with magnetic resonator coupling and sleep/active strategy for a drone charging station in smart agriculture," *IEEE Access*, vol. 7, pp. 139839–139851, 2019.

[15] C. Rong et al., "Critical review of recent development of wireless power transfer technology for unmanned aerial vehicles," *IEEE Access*, vol. 11, pp. 132982–133003, 2023.

[16] C. Xia et al., "Design and optimization of the three-phase rail-type magnetic coupling structure for the electric vehicle wireless power transfer system," *Elect. Eng.*, vol. 103, pp. 79–89, 2021.

[17] S. Cui, B. Song, and Z. Wang, "Overview of magnetic coupler for electric vehicles dynamic wireless charging," *Trans. China Electrotechnical Soc.*, vol. 37, no. 3, pp. 537–554, 2022.

[18] W. Li, Y. Li, Y. Shi, and C. Xia, "Study on voltage fluctuation of segmented rail-type dynamic wireless charging system," *Guangdong Electric Power*, vol. 35, no. 1, pp. 30–41, 2021.

[19] Z. Li, M. Tang, B. Xie, Y. Zhu, X. Guo, and H. Sun, "A study of magnetic coupling characteristics of dual receiver coil for dynamic wireless power transfer," *IEEE Access*, vol. 10, pp. 70516–70525, 2022.

[20] C. Zhang, W. Wang, C. Xu, and J. Yang, "Research on uniform magnetic field compensation structure of array circular coils for wireless power transfer," *IEEE Trans. Magn.*, vol. 57, no. 6, Jun. 2021, Art. no. 8600205.

[21] M. Xue, Q. Yang, P. Zhang, J. Guo, and H. Hou, "Optimal design of dynamic wireless power transmitting array module in random position of robot," *Trans. China Electrotechnical Soc.*, vol. 37, no. 24, pp. 6319–6331, 2022.

[22] P. Tan, T. Peng, X. Gao, and B. Zhang, "Flexible combination and switching control for robust wireless power transfer system with hexagonal array coil," *IEEE Trans. Power Electron.*, vol. 36, no. 4, pp. 3868–3882, Apr. 2021.

[23] X. Li, J. Hu, H. Wang, X. Dai, and Y. Sun, "A new coupling structure and position detection method for segmented control dynamic wireless power transfer systems," *IEEE Trans. Power Electron.*, vol. 35, no. 7, pp. 6741–6745, Jul. 2020.

[24] X. Zhang, W. Xu, F. Wang, Z. Yuan, and Q. Yang, "Research on self-decoupling segmented guide rail and dual-mode switching strategy of dynamic wireless charging system," *Proc. Chin. Soc. Elect. Eng.*, pp. 1–4, 2023.

[25] X. Zhang, J. Wang, and Q. Yang, "Study on power coupling mechanism and switching control of electric vehicle dynamic wireless power supply system," *Trans. China Electrotechnical Soc.*, vol. 34, no. 15, pp. 3093–3101, 2022.

[26] R. Senju, H. Omori, D. Uchimoto, T. Morizane, and N. Kimura, "A new position detecting method for wireless EV chargers," in *Proc. 8th Int. Conf. Renewable Energy Res. Appl.*, 2019, pp. 810–814.

[27] C. Cai, M. Saeedifard, J. Wang, P. Zhang, J. Zhao, and Y. Hong, "A cost-effective segmented dynamic wireless charging system with stable efficiency and output power," *IEEE Trans. Power Electron.*, vol. 37, no. 7, pp. 8682–8700, Jul. 2022.

[28] Z. Wang, X. Wei, and H. Dai, "Nested three-layer optimisation method for magnetic coils used in 3 kW vehicle-mounted wireless power transfer system," *IET Power Electron.*, vol. 9, no. 13, pp. 2562–2570, 2016.

Ming Xue received the B.S. and M.S. degrees from Tianjin Polytechnic University, Tianjin, China, in 2011 and 2014, respectively, and the Ph.D. degree in electrical engineering from the Hebei University of Technology, Tianjin, China, in 2022.

He is currently an Assistant Professor with the School of Electrical Engineering, Hebei University of Technology, Tianjin. His current research interests include wireless power transfer technology and its application.

Yanjie Guo (Member, IEEE) received the Ph.D. degree in electrical engineering from the Institute of Electrical Engineering, Chinese Academy of Sciences (IEECAS), Beijing, China, in 2013.

He was with the Key Laboratory of Power Electronics and Electric Drives, IEECAS. He is currently an Associate Professor with the State Key Laboratory of Reliability and Intelligence of Electrical Equipment, Hebei University of Technology. His research interests include wireless power transfer, power electronics, energy storage, battery management, microgrid, parameter identification, and electromagnetic compatibility.

Weida Xu received the B.S. degree in electrical engineering and automation from the Hebei Agricultural University, Hebei, China, in 2021. He is currently working toward the M.E. degree in electrical engineering with the Hebei University of Technology, Tianjin, China.

His research interests include engineering electromagnetism, wireless power transfer, and its industrial applications.

Yibo Gao received the B.S. degree in building electric technology from the Hebei University of Architecture, Hebei, China, in 2021, and the M.S. degree in electrical engineering from Tiangong University, Tianjin, China, in 2024.

His research interests include wireless power transfer and its industrial applications.

Shengyan Qiu received the B.S. degree in electrical engineering and automation from the Hebei Agricultural University, Hebei, China, in 2021. He is currently working toward the M.E. degree in electrical engineering with the Hebei University of Technology, Tianjin, China.

His research interests include engineering electromagnetism, wireless power transfer, and its industrial applications.